

Spyros Tsentis¹, Ioannis Goulos¹, Simon Prince¹, Vassilios Pachidis¹ & Vladeta Zmijanovic²

¹Cranfield University, Bedfordshire MK43 0AL, UK ²Reaction Engines Ltd., Culham Science Centre, Abingdon OX14 3DB, UK

Abstract

This paper presents a numerical investigation on the base flow characteristics of a sub-scale, high-speed exhaust system at over-expanded state. The geometry is representative of future, advanced propulsion concepts. It features a truncated, ideal-contoured (TIC) nozzle and an axisymmetric cavity embedded at the base. Scale resolving simulations are performed using the Delayed Detached Eddy Simulation (DDES) turbulence modelling approach. The configuration is mounted on the test section of a wind tunnel through a wing-pylon to facilitate ongoing experiments. The proper orthogonal decomposition (POD) method is employed to identify the salient flow features at the base in terms of energy content. Time-averaged base pressure results show slightly reduced levels of pressure behind the pylon by approximately 1.2%. Additionally, reduced levels of pressure fluctuations in the region directly downstream of the pylon are identified, suggesting a severe impact on the base flow. This is further confirmed through the modal decomposition of the base flow. The first two most energetic modes of the flow exhibit strong spatial asymmetry in the intensity of velocity fluctuations, the latter being significantly reduced in the region behind the pylon. This is important for future, high-speed vehicles, which typically employ wingtip mounted nacelles and could exhibit increased levels of side loads as a result of this azimuthal asymmetry in the flow development.

Keywords: base flow, high-speed exhausts, base drag, DDES, POD

1. Introduction

1.1 Background

Future propulsion systems can enable routine space access as well as sustainable, high-speed, intercontinental travel capabilities. Most of these concepts found in the open literature focus on ram air compression like ramjets [1] and scramjets [2]. However, these systems cannot generate static thrust and therefore, combined-cycles have also been developed, including turbine-based and rocket-based systems [3, 4]. In such configurations, two (or more) propulsion architectures are combined to provide continuous operation from sea-level static conditions up to supersonic and hypersonic speeds.

Another promising technology for re-usable, high-speed flight and space access, lies in the concept of pre-cooled, combined-cycles [5]. In these systems, a pre-cooling technology is incorporated to cool down the incoming air prior to compression, thus expending the operational range of the downstream turbomachinery. Such systems have been studied extensively in previous studies from a conceptual design perspective [6], and have been found to outperform contemporary chemical rockets in terms of performance [7, 8]. While their thermodynamic efficiency advantage is well-established, their aerodynamic behavior is not yet well understood, especially at the base region, where massive flow separation occurs.

These concepts usually feature high-speed, convergent-divergent nozzles embedded at the base [9]. This poses notable differences compared to contemporary launch vehicles, where the propulsive nozzle typically juts out of the vehicle's base. This is usually simplified in most of the reported studies,

and represented in terms of flow physics, with axisymmetric, backward facing step (BFS) topologies. Additionally, owing to the embedded nozzle design, such systems usually feature cavity regions to facilitate nozzle operation and gimballing motion, therefore requiring further assessment of the cavity impact on the propulsion aerodynamics [9]. Furthermore, most of these concepts are typically employed in high-speed, spaceplane-like vehicles using wingtip-mounted configurations [10], which create the need to investigate the impact of the wing on the base flow behavior, especially at overexpanded nozzle conditions.

1.2 Characteristics of propulsive base flows

The flow separation that takes place at the base of launch vehicles and propulsion systems can have a significant effect on the nozzle as well as on the overall aerodynamic performance, the latter being strongly related to base drag [11]. The flow characteristics at the base of launch vehicles have been extensively studied over the years for both planar and axisymmetric geometries. Most of the studies found in the public domain focus on blunt-based bodies of revolution [12, 13] and BFSs [14, 15] for both powered-on [14] and powered-off [13] conditions. As mentioned previously, the wide use of axisymmetric BFS configurations is directly related to the design of most contemporary rocket-based transportation systems, where the propulsive nozzle extends downstream of the base. This geometry can be simplified and represented in terms of base flow physics, with a BFS configuration. Studies on more detailed geometries can also be found, such as the effect of side boosters on the base flow of cylindrical BFS configurations using both experimental [16] and numerical [17] activities, at subsonic conditions of M_{∞} =0.7. Significant increase in the coefficient of base pressure fluctuations was reported of approximately 45% as a result of the presence of the boosters, indicating the critical effect of base geometry on the propulsion aerodynamics. Additionally, results on the base flow characteristics and side loads of more detailed geometries of the European launchers Ariane5 and Vega, can be found in the study of Schwane [18]. While many studies have been conducted on such BFS-like configurations, future, high-speed systems, as those discussed earlier, could feature base geometries where the nozzle does not jut out of the base [9]. Analyses on exhaust systems with base-embedded nozzle(s) and cavity regions have not been reported in previous studies.

Base cavities in specific have been typically studied for base drag reduction in the context of base flow control [19]. They belong to the family of passive flow control mechanisms for base pressure modification, including locked vortex afterbodies and boat tailing [12, 19], among others. The interested reader is referred to a comprehensive review on flow control mechanisms for base drag reduction provided by Tanner [20]. It is well-established that base cavities are effective for base drag reduction, but their effectiveness is a function of the ratio l_c/D , where l is the cavity length and D is the diameter of the base of the body [21]. Most of the studies found in the public domain on base cavities are in the context of base flow control. However, future, high-speed propulsion systems will feature base cavities as an integral design aspect necessary for successful operation. Cavities will be required to allow space for nozzle gimballing and/or heat load protection capabilities. While the authors have demonstrated the significant impact such cavities could pose on the nozzle and base aerodynamics in previous work [9], further studies are required using both numerical and experimental analyses. Additionally, such systems usually feature a wingtip-mounted nacelle topology [10], and therefore, the fundamental impact of the attached wing on the base flow dynamics of the exhaust system must be examined and quantified, especially at over-expanded nozzle states where side loads are critical [22]. Studies on this issue are currently scarce in the open literature.

1.3 Scope of present study

This paper presents a numerical investigation on the base flow characteristics for a sub-scale, high-speed exhaust system at over-expanded nozzle conditions. The geometry is representative of future, advanced propulsion concepts and features a TIC nozzle and an axisymmetric cavity region embedded at the base. The examined, sub-scale model is mounted on the side wall of a transonic tunnel configuration to facilitate ongoing experiments. The Delayed Detached Eddy Simulation (DDES) turbulence modelling approach is adopted, owing to its global nature and reduced computational cost for wall-bounded flows. The conditions examined correspond to a tunnel pressure ratio of 1.28, giving an approach Mach number of approximately 0.5 at the tunnel inlet, while the nozzle pressure ratio

is 10, and the nozzle is at Free Shock Separation (FSS) state. The impact of the wing-pylon on the unsteady flow features at the base is analysed by means of time-averaged and fluctuating base pressure distribution. The proper orthogonal decomposition method is employed to further examine the base flow dynamics and the impact of the wing on the flow organization at the base through the most energetic POD modes is identified and reported. Studies on the unsteady base flow characteristics of similar high-speed exhaust systems have not been reported in the public domain.

2. Methodology

2.1 Sub-scale exhaust model description

This study facilitates an experimental campaign that is currently ongoing. Figure 1 shows a schematic of the sub-scale model that is mounted on the test section of the transonic wind tunnel (TSWT) of the Defence Academy of the United Kingdom. The wind tunnel is a closed-circuit, ejector-driven configuration and has a working test section of Hxh=0.228x0.207 m². The tunnel features solid walls without perforation and the blockage caused by the model is approximately 16.5%. This makes resolution of the boundary layer at the tunnel walls important for the numerical simulations. The conditions of the flow in the wind tunnel are controlled through the regulation of the ejectors pressure, herein denoted as p_{out} , while the total pressure approaching the model $(P_{0,t})$ is nearly atmospheric. The tunnel pressure ratio (TPR) that is used to set the flow conditions is defined as $TPR=(P_{0,t}/p_{out})$.

The model consists of an ogive-shaped nose and a main cylindrical body, which form the nacelle surface (Fig. 1). It features a high-speed, TIC nozzle embedded at the base, along with an axially symmetric cavity region located between the nozzle and the nacelle. The cavity has a length of l_c/D =0.95 and a corresponding thickness of 0.0875D, where D is the maximum model diameter. The model is mounted on the right side tunnel wall through a pylon which features a NACA 0026 profile cross-section. The maximum pylon thickness and length, non-dimensionalized over the model diameter, are approximately 0.46 and 1.77, respectively. The wall contour of the nozzle in the divergence is generated using the axisymmetric Method of Characteristics (MoC) procedure [23] to get a shockless flow expansion. The near-critical conditions at the throat are approximated by employing Sauer's method [24], and used as an initial value line for the MoC procedure. The final ideal contour is then truncated at an angle of 7.6 degrees, thus producing a design exit Mach number of approximately 3.4 and a design nozzle pressure ratio of NPR=59.

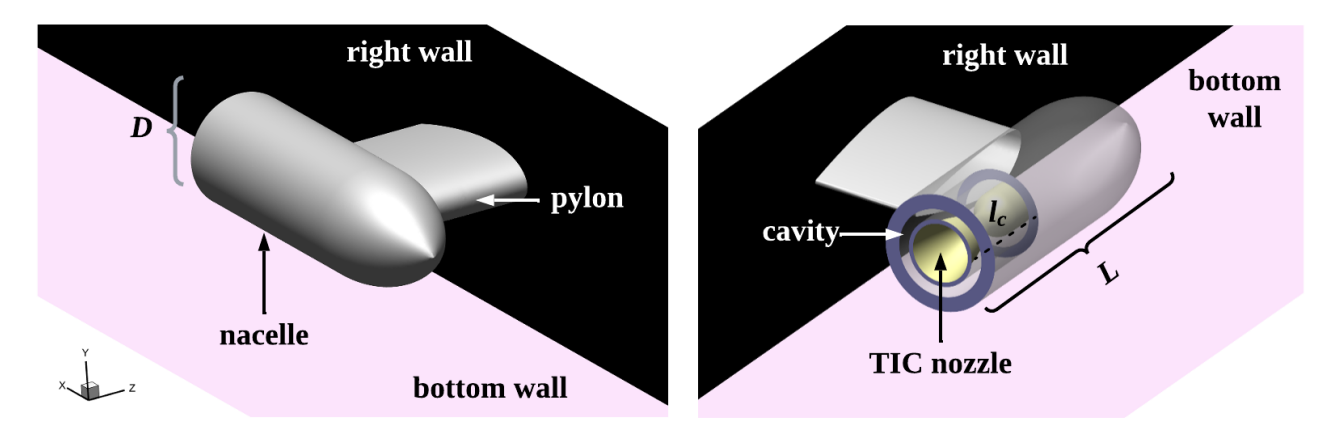


Figure 1 – Schematic of the mounted model and test-section

2.2 Computational approach

The employed model solves the Reynolds-averaged version of the three-dimensional Navier-Stokes equations, describing the conservation of mass, momentum and energy (Eqs. (1)- (3)). Due to compressibility effects, the mass-weighted equations or Favre-averaged are considered [25].

$$\frac{\partial \rho}{\partial t} + \frac{\partial (\rho u_i)}{\partial x_i} = 0 \tag{1}$$

$$\frac{\partial(\rho u_i)}{\partial t} + \frac{\partial(\rho u_j u_i)}{\partial x_j} + \frac{\partial p}{\partial x_i} - \frac{\partial(t_{ij} + \rho \tau_{ij})}{\partial x_j} = 0$$
 (2)

$$\frac{\partial(\rho E)}{\partial t} + \frac{\partial(\rho u_j E + \rho u_j)}{\partial x_i} - \frac{\partial(u_i(t_{ij} + \rho \tau_{ij}))}{\partial x_i} + \frac{\partial q_j}{\partial x_i} = 0$$
(3)

In the equations above, ρ is the fluid density, u_i is the velocity component in the ith direction, E is the total energy per unit mass and q_j is the heat-flux vector. The total stress tensor, is the sum of the viscous stress tensor, denoted as t_{ij} , and the Reylonds stress tensor $\rho \tau_{ij}$, which is defined based on the Boussinesq approximation [25].

Owing to the wall-bounded flow topology and the high Reynolds number ($Re_D = 0.85 \cdot 10^6$ at the tunnel inlet and $1.03 \cdot 10^6$ at the vicinity of the base), the selected turbulence modelling approach in this work is the Delayed Detached Eddy Simulation (DDES) [26], which belongs to the family of hybrid RANS/LES methods [27]. The implementation of DDES in this work is based on the $k-\omega$ shear stress transport (SST) eddy viscosity model, as introduced by Menter [28]. This model solves two additional transport equations for the turbulent kinetic energy k and specific dissipation rate ω as shown in Eqs. (4), (5). The full mathematical formulation of the model is not repeated here for brevity. The interested reader is referred to [28].

$$\frac{\partial(\rho k)}{\partial t} + \frac{\partial(\rho u_i k)}{\partial x_i} = \widetilde{P}_k - \beta^* \rho k \omega + \frac{\partial}{\partial x_i} \left[(\mu + \sigma_k \mu_t) \frac{\partial k}{\partial x_i} \right]$$
(4)

$$\frac{\partial(\rho\omega)}{\partial t} + \frac{\partial(\rho u_i\omega)}{\partial x_i} = a\rho S^2 - \beta\rho\omega^2 + \frac{\partial}{\partial x_i} \left[(\mu + \sigma_\omega \mu_t) \frac{\partial\omega}{\partial x_i} \right] + 2(1 - F_1)\rho\sigma_{\omega 2} \frac{1}{\omega} \frac{\partial k}{\partial x_j} \frac{\partial\omega}{\partial x_j}$$
(5)

The dissipation term of the turbulent kinetic energy in the formulation of the $k-\omega$ SST model is modified in the DDES approach as described in [29, 30]. The transport equation of k in this formulation reads as:

$$\frac{\partial(\rho k)}{\partial t} + \frac{\partial(\rho u_i k)}{\partial x_i} = \frac{\partial}{\partial x_i} \left[(\mu + \sigma_k \mu_t) \frac{\partial k}{\partial x_i} \right] + \widetilde{P}_k - \rho \sqrt{k^3} / l_{DDES}$$
 (6)

The DDES length scale is defined as follows:

$$l_{DDES} = l_{RANS} - f_d max(0, l_{RANS} - l_{LES})$$

$$\tag{7}$$

$$l_{LES} = C_{DES}\Delta \tag{8}$$

$$l_{RANS} = \frac{\sqrt{k}}{\beta^* \omega} \tag{9}$$

$$C_{DES} = C_{DES1}F_1 + C_{DES2}(1 - F_1)$$
(10)

where C_{DES1} =0.78 and C_{DES2} =0.61 are calibration constants, and Δ is the maximum local grid spacing

 $(\Delta = \max(\Delta_x, \Delta_y, \Delta_z)$ in a Cartesian grid). The shielding function that protects the boundary layer from the DES limiter in the DDES approach is obtained as,

$$f_d = 1 - \tanh\left[\left(C_{d1} \frac{v + v_t}{\kappa^2 y^2 \sqrt{0.5(S^2 + \Omega^2)}}\right)^{C_{d2}}\right]$$
 (11)

where S and Ω is the magnitude of the strain rate and vorticity tensors, respectively, y is the distance to the nearest wall surface; κ is the von Kármán constant and C_{d1}, C_{d2} , are constants equal to 20 and 3 respectively [30]. In the original DES formulation that was introduced by Spalart (known as DES97) [31], as well as in the DES-SST formulation, there is no mechanism to prevent the DES limiter of activating inside the attached boundary layers when the local grid spacing at the wall surface gets smaller than the boundary layer thickness ($\Delta < c\delta$, where c is order one). This leads to reduced modeled Reynolds stresses and excessive eddy viscosity reduction in the switch area (or "gray" area), causing what is known as modeled stress depletion (MSD) behavior as identified early on by Menter and Kuntz [32]. In such cases, the limiter is activated in the boundary layer, and results in grid-induced flow separation. The introduction of the blending function (Eq. (11)) serves as a modification of the original DES formulation and ensures that the solver remains in RANS mode in attached boundary layer regions, even under severe grid refinement, which would otherwise activate the DES limiter. This improves the solution behavior and prevents excessive reduction of the eddy viscosity in the switch area.

A compressible, density-based and implicit solver [33] is used for the computations. A second order upwind scheme is employed for spatial discretization of the flow primitive and turbulent variables (turbulent kinetic energy and specific dissipation rate). We note that the use of less dissipative schemes, usually preferable for classical LES arppoaches, such as the bounded-central-differencing (BCD) scheme, led to numerical stability issues [34, 35]. The Advection Upstream Splitting Method (AUSM+) is employed for calculation of the inviscid fluxes [36] and a least-squares cell-based method is used for calculation of the flow-field gradients due to the polyhedral topology of the employed grid, leading to increased computational cost for a node-based approach (see Fig. 3). Air is modeled as an ideal gas, due to the cold-flow nozzle tests. The specific heat capacity at constant pressure C_p is computed using an 8^{th} order piece-wise polynomial as a function of static temperature, while thermal conductivity is obtained based on kinetic theory [33]. The dynamic viscosity is calculated using Sutherland's law [37]. A second order accurate, backward scheme is employed for time integration. Further details on the accuracy of the employed solver on a number of severe base flow separation cases using scale-resolving simulations can be found in [34].

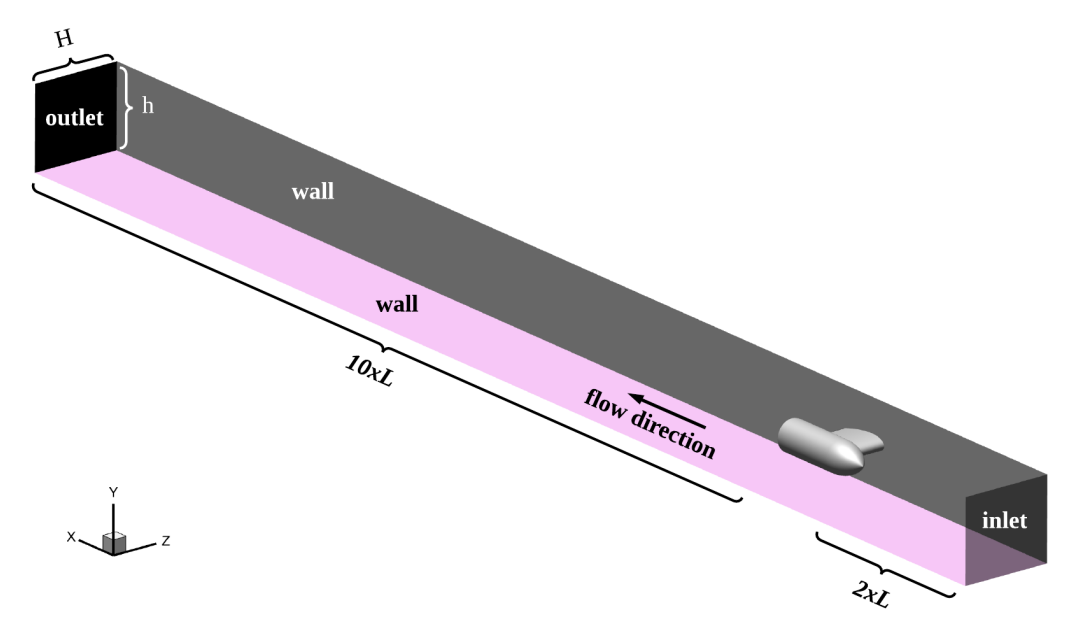


Figure 2 – Computational domain of the sub-scale model installed in the TSWT test section

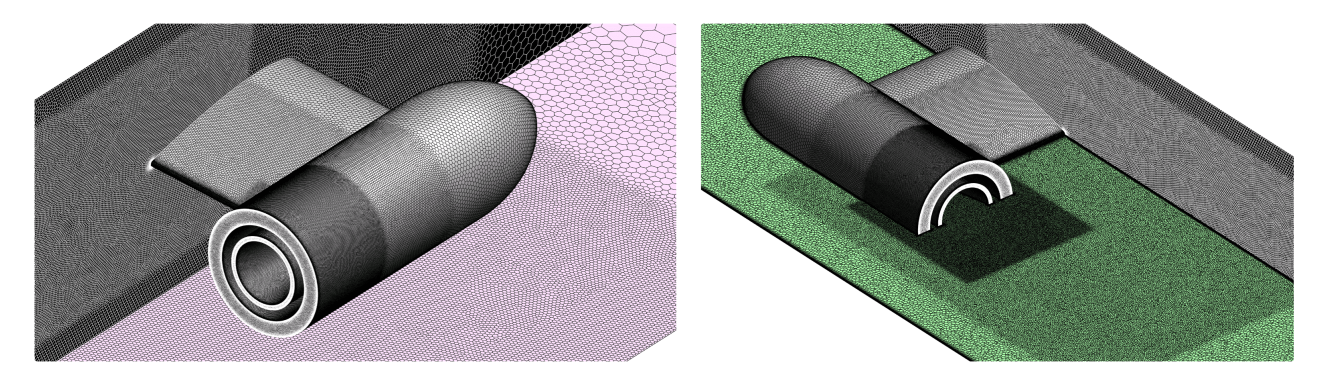


Figure 3 – Computational mesh

Figure 2 depicts the computational domain employed for the numerical simulations. The domain consists of the working test section of the wind tunnel (Hxh), which is extended by 10 times the model's length L downstream of the base and 2 times upstream. The other two test section walls are hidden in Fig. 2 for visibility reasons. The flow conditions at the tunnel inlet are modeled by applying a pressure inlet boundary condition (BC), where the total pressure and temperature are prescribed. At the tunnel outlet, a pressure outlet BC is applied, imposing the static pressure value. The nozzle conditions are modeled through the application of a pressure inlet BC at the nozzle inlet, prescribing the total pressure and temperature. Due to the cold flow tests, the total temperature at the nozzle inlet is set to 290 K. Owing to the high blockage, flow conditions vary throughout the domain. Therefore, for consistency, the nozzle pressure ratio (NPR), is defined as the nozzle inlet total pressure $P_{0,n}$, over the tunnel outlet static pressure $P_{0,n}$. All wall surfaces of the model, pylon and tunnel are treated with viscous, no-slip and adiabatic wall BCs. The computations are performed for conditions of TPR=1.28 and NPR=10, which corresponds to over-expanded nozzle operation featuring a Free Shock Separation state (FSS) [38] with a typical Mach-disk reflection.

The domain is discretized using a hybrid meshing approach [39]. Grid convergence is intricate in scale-resolving simulations compared to pure RANS and DNS (Direct NUmerical Simulation) approaches, due to the filtering operation performed on the Navier-Stokes equations, as emphasized by Spalart in [40]. Herein, a precursor RANS solution is used to initialize the unsteady part of the computation. Consequently, the meshing approach adopted in this work, is initially informed from previous work [41], where a second order Grid Convergence Index (GCI) [42] study is performed based on the generalized Richardson extrapolation [43]. The GCI corresponding to the medium mesh for the nozzle velocity coefficient C_V and the Gross Propulsive Force (GPF) [41] was 0.42% and 0.68%, respectively. The apparent order p was close to the formal order of the employed scheme, which is a good indication for the asymptotic behavior of the grids. Grid convergence must be demonstrated for the part of the domain where the model acts in RANS mode, and therefore, this meshing approach forms the baseline for this study. It is specifically important that all of the boundary layers of interest are sufficiently resolved [34]. The baseline grid is then further refined at the base and near-wake regions to improve resolution. This region can be treated as the "focus region" as discussed in [40]. The maximum cell size in that region is 0.23 δ , where δ is the 99% boundary layer thickness just upstream of the model's base, and is evaluated from precursor RANS simulations. The employed cell size in that region ensures that the ratio of the local grid size Δ_{max} over the RANS length scale (Eq. (9)) is small enough to allow proper resolution of the initial instability of the separating shear layer from the base. The final employed computational mesh is depicted in Fig. 3 and has values of (Δ_{max}/l_{RANS}) well below 0.1 as recommended in [34]. The refinement region extends one diameter D downstream of the base and covers the cavity region upstream. A total of 35 prism layers are employed, ensuring a non-dimensional distance of y^+ below 1 for all wall-adjacent nodes. The remainder of the domain is discretized using polyhedral elements, which are usually more efficient compared to tetrahedrons in terms of cell-count. The final grid comprises a total 25 million cells.

The physical time step of the simulation is set to $\Delta t = 2 \cdot 10^{-5}$ s. It is selected as such to ensure that the local Courant-Friedrichs-Lewy (CFL) number is below 1 in most of the scale-resolving part of

the domain. This is facilitated through the assessment of the local time scales based on a precursor RANS simulation [34], as $\Delta/|U|$, where |U| is the local velocity vector and Δ is the grid spacing approximated as $(\Delta x \Delta y \Delta z)^{(1/3)}$. An additional analysis aimed at resolving the global unsteady dynamics of the shedding frequency of large-scale structures at $St_D=0.2$ (where $St_D=fU/D$ denotes the Strouhal number) showed that the employed time step size is sufficient. CFL values up to 8 were reached in the supersonic jet boundary and 35 in the attached boundary layer of the divergent section of the nozzle. Reducing the time step size further to maintain the CFL below 1 in majority of the wake flow, increased the computational cost to impractical values with current resources. After an initial transient phase, the unsteady calculation initiates, which allows collection of statistics. The useful unsteady calculation is performed over a period of T=0.2 seconds. The computations are carried out on 256 CPU cores of AMD EPYC-7543 processors of the high performance computing facilities of Cranfield University and have a total computational cost of approximately 0.2 Mio CPU hours.

3. Results

3.1 Salient base flow features

The instantaneous flow characteristics at the base are depicted in Fig. 4, where coherent structures are identified through the use of positive iso-surfaces of the Q-criterion [44], defined as the second invariant of the velocity gradient tensor ∇u :

$$Q = \frac{1}{2} \left(\Omega_{ij} \Omega_{ij} - S_{ij} S_{ij} \right) \tag{12}$$

Here Ω_{ij} and S_{ij} are the anti-symmetric and symmetric components of the velocity gradient tensor, respectively. One can notice the roll-up of azimuthal vortical structures at the base which correspond to the annular shear layer instability and grow by pairing as they move downstream. Owing to the increased blockage, the shear layer development is asymmetrical in the azimuthal direction and therefore, these vortical structures quickly lose their azimuthal coherence, unlike what can be observed in axially symmetric configurations in free-stream flow conditions [15]. Additionally, the formation of small and large scale hairpin vortices is evident, similar to what has been observed on the base flow of axisymmetric BFSs [15] and blunt-based bodies [13]. It is worth noting that the formation and development of turbulent structures takes place promptly after separation without any noticeable delay, which indicates sufficient resolution and proper activation of the scale-resolving branch. This was further examined and confirmed through the visualization of the blending function f_d (see Eq. (11)).

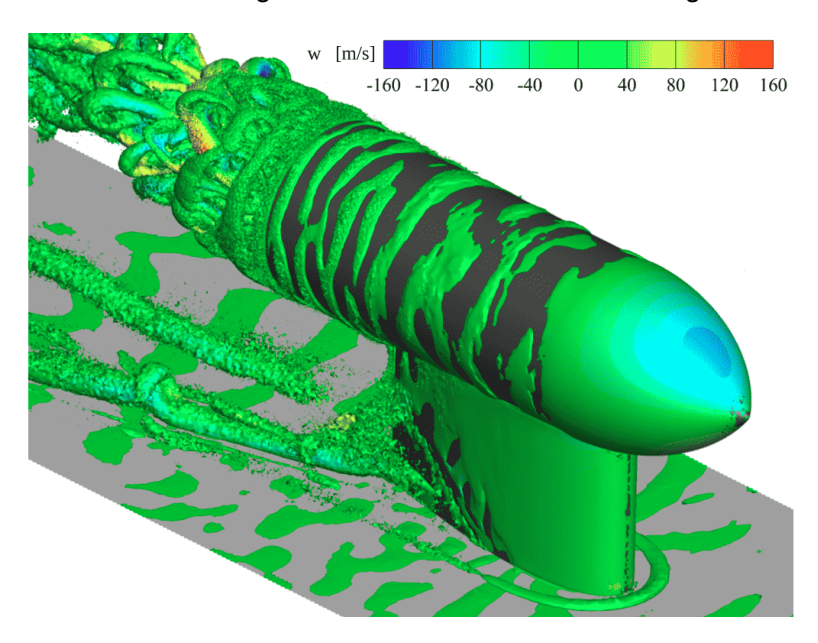


Figure 4 – Instantaneous Q-criterion coloured by spanwise velocity

The time-averaged flow-field at the base is obtained using data at discrete time instances of $10\Delta t$ and is presented in Fig. 5 along the symmetry plane (xz). Base flow organization is characterized by the

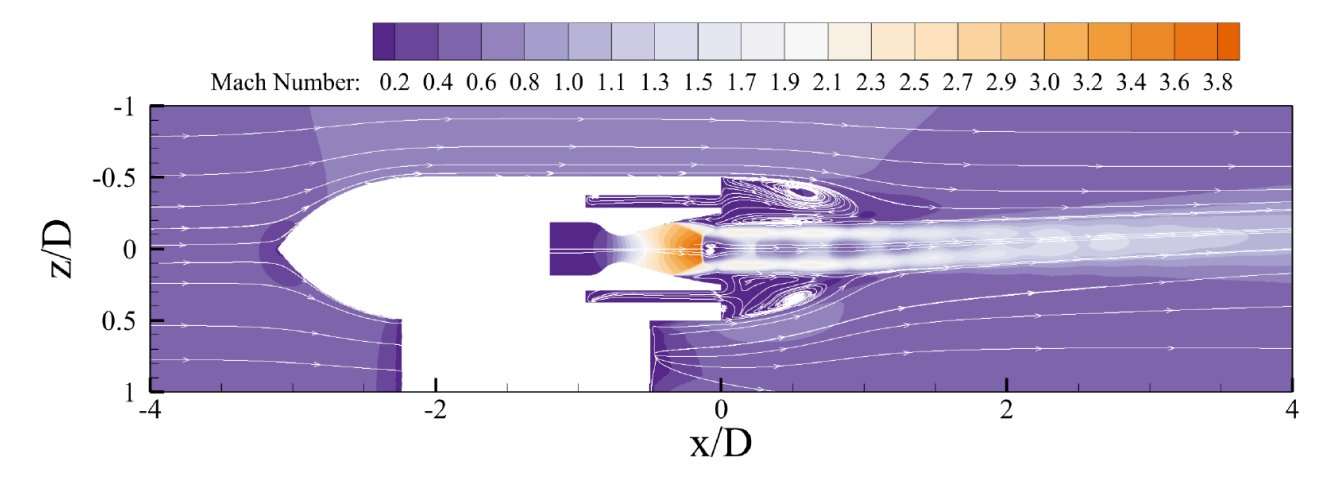


Figure 5 – Time-averaged Mach number distribution from DDES

formation of a pair of low-speed, counter-rotating recirculation regions established at the separated flow downstream of the base. A dominant, primary recirculation region appears, which is substantially larger in size compared to the secondary vortex, and is associated with the separating shear layer instability. Additionally, the asymmetrical development of the shear layer can also be seen. In specific, the shear layer is affected by the wake flow of the wing-pylon, and appears slightly shifted upwards towards the jet, suggesting a suppression effect. This is also evident through the distorted and reduced size of the secondary vortex at this location compared to the opposite side, where there is no pylon effect. The time-averaged jet flow is vectored and tilts upwards as a result of the presence of the pylon [41]. Finally, a counter-rotating vortex pair is established immediately downstream of the Mach disk, inside the subsonic region of the jet. This phenomenon has been identified in previous studies for TIC nozzles at over-expanded state using both RANS [9] and scale-resolving simulations [45]. It is related to the curvature of the Mach disk reflection and further details on its origin can be found in [38].

3.2 Base pressure distribution

Figure 6a illustrates the time-averaged pressure distribution obtained from DDES, normalized with the tunnel outlet pressure p_{out} . Superimposed are the results from the steady, RANS computation for comparison. The azimuthal locations where data is taken (i.e., 0, 90, 180 and 270 degrees) correspond to locations where dynamic pressure sensors are located in the experimental model. The radial location of the data points is r/R=0.875, where R is the base radius (D/2). This location is in the middle of the base wall surface (see Fig. 1). It is shown that the mean base pressure calculated from both DDES and RANS, is slightly reduced behind the pylon (i.e., 180 degrees), while the pressure levels in the xy plane (symmetry plane - 90° and 270°) are similar. The pressure is slightly reduced by 1.2% at 180° compared to 0° (xz plane), indicating the pressure asymmetry caused by the wing-pylon. Additionally, it is worth noting that the difference in base pressure between RANS and DDES calculation is below 3%, and that the trend is properly captured with RANS, which indicates that RANS can be used with confidence, especially at the conceptual design phase, where computational cost of scale-resolving simulations is prohibitive.

Figure 6b shows the coefficient of the root-mean-square value of the pressure fluctuations, defined as $p'=p-\overline{p}$. This is useful to examine the unsteady behavior of base pressure, which cannot be revealed through time-averaging. The definition of this coefficient is $C_{p_{rms}}=\sqrt{\overline{p'^2}}/q_{\infty,0}$, where q is the dynamic pressure and the subscript $(\infty,0)$ denotes the flow conditions at the vicinity of the base and 0° azimuthal angle as defined in Fig. 6b The level of base pressure fluctuations at 90° and 270° is reduced by approximately 20% compared to 0° . This is a result of the three-dimensionality of the flow examined. In particular, the distance of the model's base from the test section walls in the xy plane is smaller than the equivalent distance in the xz plane. Additionally, the presence of the pylon affects the afterbody flow characteristics in the xy plane compared to the free-stream side at 0° in the xz

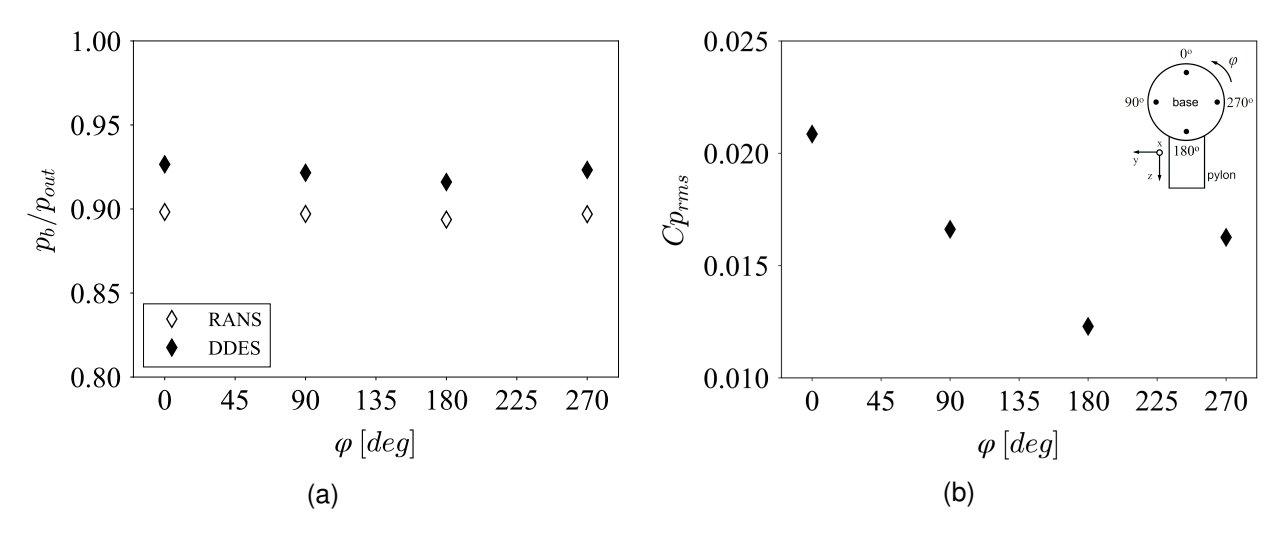


Figure 6 – Time-averaged base pressure distribution (a); coefficient of the rms of base pressure fluctuations (b)

plane. The base pressure fluctuations behind the pylon are further reduced by approximately 26% compared to the 90° and 270°. This indicates that the characteristics of the separating shear layer at that location are strongly impacted as a result of the wake of the pylon compared to the opposite, free-stream side. This strong asymmetry in the base pressure distribution as a result of the wing-pylon can give rise to side loads on the exhaust system, in the plane parallel to the wing. Once again the symmetry of the flow is evident in the xy plane, with $C_{p_{rms}}$ exhibiting similar values at azimuthal locations of 90° and 270°.

3.3 Proper orthogonal decomposition

Modal decomposition methods can be employed for numerical or experimental data, to further analyse aerodynamic flows and try to extract physically important features or modes. The Proper Orthogonal Decomposition (POD) is employed herein to investigate the salient features of the base flow.

3.3.1 Formalism

The proper orthogonal decomposition is a modal analysis technique that was first introduced into the fluid dynamics community by Lumley [47] as a mathematical tool to extract coherent structures from a set of flow-field data. It provides an algorithm that allows to decompose the original data set into a minimal number of basis functions or modes which are orthogonal, and maximize the energy captured. A more detailed analysis of POD can be found in [48], while a review of modal decomposition techniques for fluids can be found in the study of Taira et al. [49].

The input data in the POD are snapshots of any scalar or vector field $\mathbf{q}(\mathbf{x},t)$ over discrete spatial points x at discrete time instances t_i . The fluctuations in the original flow are expressed as a linear combination of the spatial modes and their corresponding temporal coefficients as:

$$\mathbf{q}'(\mathbf{x},t) = \mathbf{q}(\mathbf{x},t) - \overline{\mathbf{q}}(\mathbf{x}) = \sum_{k=1}^{\infty} a_k(t) \Phi_k(x)$$
(13)

Herein, POD is performed over a total of 5000 snapshots, equally spaced in time with $\Delta t = 2 \cdot 10^{-5}$ s corresponding to a total flow-time of 0.1 s. Planar data is monitored and stored along xz plane during the computation. The data is then processed to reduce the "POD window" to the region of interest in the base and to reduce computational and storage costs. The window of the base flow where POD is performed, forms a rectangular centered around (x, z)=(0, 0). It extends from the nozzle inlet upstream of the base up to 1.25D downstream in the wake region, while it spans a length of 2.2D up and down in the z direction. The method employed in this work for performing the POD is based on calculating the singular value decomposition (SVD) of the original snapshot matrix X, containing the

fluctuating part of the z-velocity component. This snapshot matrix is obtained from the instantaneous flow-field data $\mathbf{w}'(\mathbf{x},t)$, after subtracting its time-averaged value, denoted as $\overline{\mathbf{w}}(\mathbf{x})$ (Eq. (13)). The SVD can be performed on a rectangular matrix to get the left and right singular vectors, or in matrix form, the decomposition reads:

$$\mathbf{X} = \mathbf{U}\Sigma\mathbf{V}^T \tag{14}$$

where **U** and **V** contain the left and right singular vectors of **X** and Σ contains the singular values along its diagonal. These singular vectors are identical to the eigenvectors of the correlation matrices $\mathbf{X}\mathbf{X}^T$ and $\mathbf{X}^T\mathbf{X}$ related to the direct and snapshot methods of computing the POD, respectively [49]. Additionally, the singular values are related to the eigenvalues as $\sigma_i^2 = \lambda_i$. In other words, SVD can be directly applied to the original snapshot matrix **X** to obtain the POD modes [49].

3.3.2 POD results

With these provisions, the distribution of energy captured by each mode is depicted in Fig. 7 for the first 200 POD modes. It is found that the first two modes capture approximately 11% and 8% of the energy in the base flow, while around 100 modes are required to capture energy levels above 90% of the flow. This is unlike to a number of canonical aerodynamic flows where usually a few modes can capture most of the energy [48, 50] and serve to construct reduced-order models. This behavior is diminished as the geometry gets more complex and the multi-scales of turbulence involved are harder to extract.

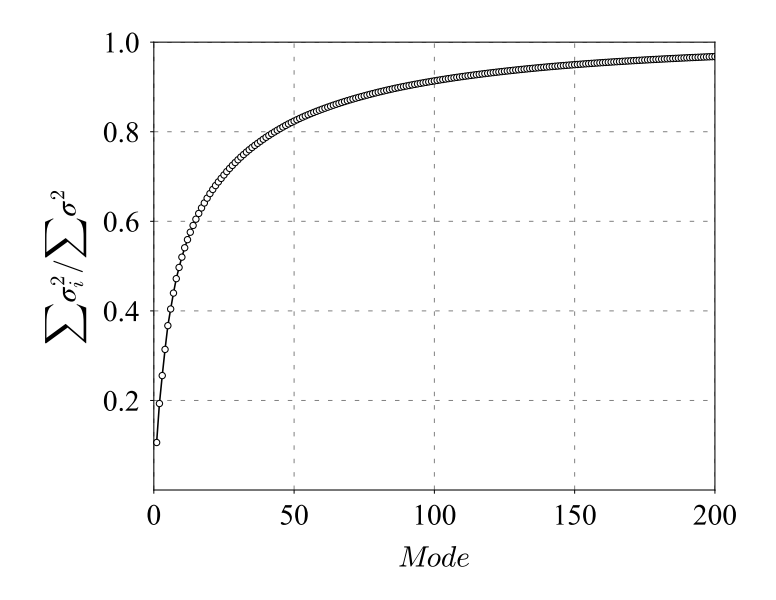


Figure 7 – Cumulative energy content with increasing number of POD modes

Figure 8 shows the first two, most energetic POD modes of the z-velocity fluctuations in the flow near the base and wake regions. The modes show zones of velocity correlations, representing coherent structures in the wake. One can notice that these modes are similar but appear shifted in the flow direction, which is typically a manifestation of travelling structures by a pair of stationary POD modes [49]. Additionally, it is clearly demonstrated that the most dominant modes feature strong asymmetry in the energy levels in the xz plane. In specific, the region downstream of the wing-pylon exhibits weak levels of velocity fluctuations compared to the top side of the base. This clearly shows that the development of flow unsteadiness is being suppressed in the region behind the pylon, in line with the results shown visually in Fig. 5 and quantified in Fig. 6b. This strong asymmetry which manifests in the most energetic POD modes can lead to asymmetric side loads generated on the exhaust system. This type of wingtip-mounted nacelles is typically found in future, high-speed vehicles [10], and therefore further analyses should be carried out to examine this effect in more realistic configurations to take actual installation effects into account (e.g., the size/thickness of the wing, swept-wing configuration etc.). Still, this analysis suggests that the effect of the wing-pylon could be quite important on the base flow for future, high-speed exhausts.

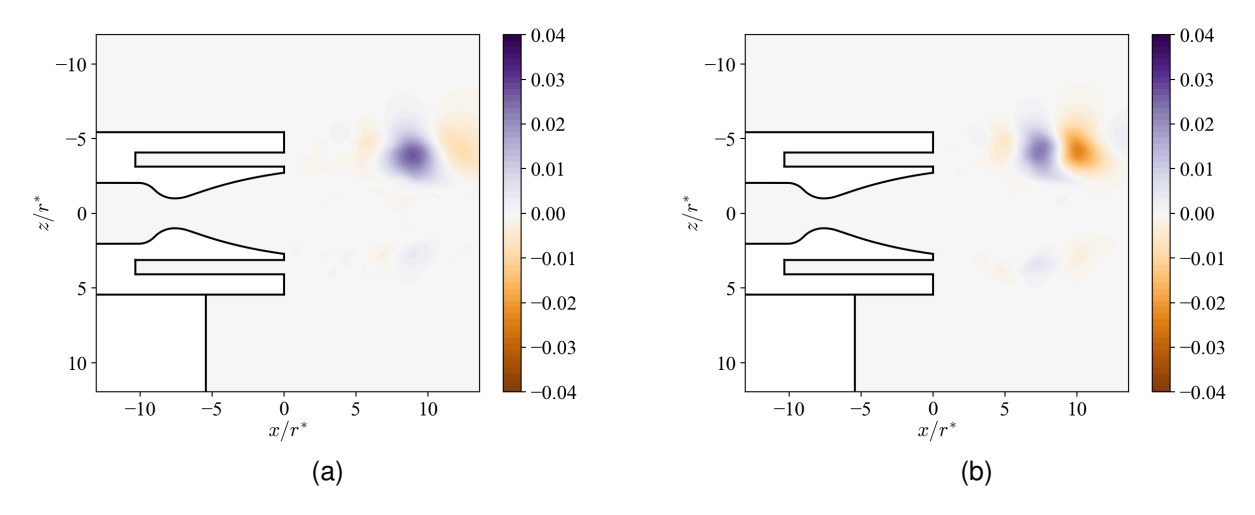


Figure 8 – First two leading POD modes; (a) 1^{st} mode, (b) 2^{nd} mode

4. Conclusions and future work

This paper presented the salient flow characteristics at the base of a representative, sub-scale and high-speed exhaust system at over-expansion state. The geometry features a TIC nozzle and a cavity region embedded at the base, which will be essential for proper operation of such advanced propulsion systems in the future. The Delayed Detached Eddy Simulation turbulence modelling approach is employed in this work, owing to its reduced computational cost for wall-bounded flows. The impact of the wing-pylon on the base pressure distribution has been analyzed in time-averaged as well as unsteady manner. The mean base pressure directly downstream of the pylon is slightly reduced by approximately 1.2%. The RANS results agree with the time-average DDES computation in terms of base pressure within 2-3% depending on the azimuthal location, and properly capture the trend, suggesting that RANS can be employed with relative confidence in such geometries if only the mean flow characteristics are of interest. Additionally, the fluctuating component of base pressure is examined and shown to be notably reduced behind the pylon. This suggests that the asymmetrical levels of pressure fluctuations at the base could give rise to undesirable side loads in the plane parallel to the wing as a result of its presence. These results were further confirmed through the modal decomposition of the base flow in the wing-parallel plane. In specific, the proper orthogonal decomposition method was performed on the fluctuations of the z-velocity component at the base and near-wake regions. The two leading POD modes, which together account for almost 20% of the energy in the base flow, feature strong spatial asymmetry, with the region behind the pylon exhibiting notably weaker zones of velocity fluctuations compared to the opposite side (at 0° azimuthal angle). The results of this analysis suggest that severe flow asymmetry, ergo side loads, can develop in the base flow of wingtip-mounted engines, which are typically found in high-speed vehicles [10]. It is stressed that the examined sub-scale model was not designed to analyse the wing-engine installation effects and thus can only describe the mechanism that could generate undesirable off-axis loads on the exhaust, but does not serve to quantify their magnitude.

In future work, the soundness of the employed numerical methodology will be assessed with data from the ongoing experimental activity. Additionally, the Dynamic Mode Decomposition (DMD) will be employed to allow for the frequency content of each spatial-temporal mode to be identified. Finally, more detailed wing configurations must be examined in future studies to allow for further quantification of the wingtip-mounted engine installation effects on the base flow characteristics of high-speed exhaust systems, especially at over-expanded nozzle operation.

5. Acknowledgements

The authors would like to express their gratitude to Reaction Engines Ltd. and the Cranfield Air and Space Propulsion Institute (CASPI) for funding this project and for granting permission to publish this research.

6. Contact author details

Corresponding author: Spyros Tsentis, Email: spyros.tsentis@cranfield.ac.uk

7. Copyright statement

The authors confirm that they, and/or their company or organization, hold copyright on all of the original material included in this paper. The authors also confirm that they have obtained permission, from the copyright holder of any third party material included in this paper, to publish it as part of their paper. The authors confirm that they give permission, or have obtained permission from the copyright holder of this paper, for the publication and distribution of this paper as part of the ICAS proceedings or as individual off-prints from the proceedings.

References

- [1] Ingenito A. Subsonic Comustion Ramjet Design. Springer Nature Switcherland, 2021.
- [2] Murthy S.N.B., Curran E.T. Scramjet Propulsion. AIAA, 2001. DOI 10.2514/4.866609
- [3] Bogar T. Eiswirth E. Couch L. Hunt J. McClinton C.R. Conceptual design of a Mach 10, global reach reconnaissance aircraft. *32 Joint Propulsion Conference and Exhibition*, Florida, Paper 96-2894, 1996.
- [4] Daines R. Segal C. Combined Rocket and Airbreathing Propulsion Systems for Space-Launch Applications. *Journal of Propulsion and Power*, Vol. 14, No. 5, pp 605-612, 1998.
- [5] Varvill R. Bond A. A comparison of propulsion concepts for SSTO reusable launchers. *Journal of the British Interplanetary Society*, Vol. 56, pp 108-117, 2003.
- [6] Dai J. Zuo Q. Key technologies for thermodynamic cycle of precooled engines: A review. *Acta Astronautica*, Vol. 177, pp 299-312, 2020. DOI 10.1016/j.actaastro.2020.07.039
- [7] Tsentis S. Gkoutzamanis V. Gaitanis A. Kalfas A. Multi-platform app-embedded model for hybrid air-breathing rocket-cycle engine in hypersonic atmospheric ascent. *The Aeronautical Journal*, Vol. 125, pp 1631-1653, 2021. DOI 10.1017/aer.2021.3.
- [8] Villace F. Paniagua G. Simulation of a Combined Cycle for High Speed Propulsion. 48 AIAA Aerospace Sciences Meeting Including the New Horizons Forum and Aerospace Exposition, Florida, AIAA 2010-1125, 2010.
- [9] Tsentis S. Goulos I. Prince S. Pachidis V. Zmijanovic V. Propulsion Aerodynamics for a Novel High-Speed Exhaust System. *Journal of Eng. Gas Turb. Power*, Vol. 145, No. 12, p. 121011, 2023. DOI 10.1115/1.4063416
- [10] Mehta U. Aftosmis M. Bowles J. Pandya S. Skylon Aerospace Plane and Its Aerodynamics and Plumes. *Journal of Propulsion and Power*, Vol. 53, No. 2, pp 340-353, 2016.
- [11] Hammond W. E. Design Methodologies for Space Transportation Systems. AIAA, Virgina, 2001. DOI 10.2514/4.861734.
- [12] Tran H. Dinh Q. Chu Q. Duong Q. Pham C. Do M. Effect of boattail angle on near-wake flow and drag of axisymmetric models:a numerical approach. *Journal of Mechanical Science and Technology*, Vol. 35, pp. 563-573, 2021. DOI 10.1007/s12206-021-0115-1.
- [13] Marrioti A. Buresti G. Salvetti M. V. Connection between base drag, separating boundary layer characteristics and wake mean recirculation length of an axisymmetric blunt-based body. *Journal of Fluids and Structures*, Vol. 55, pp. 191-203, 2015. DOI 10.1016/j.jfluidstructs.2015.02.012.
- [14] Paciorri R. Sabetta F. Valenza F. Fauci R. Passaro A. Baccarella D. Base-pressure experimental investigation on a space launcher in subsonic regime. *Journal of Spacecraft and Rockets*, Vol. 50, No. 3, pp. 572-578, 2013. DOI 10.2514/1.A32283.
- [15] Deck S. Thorigny P. Unsteadiness of an axisymmetric separating-reattaching flow: Numerical investigation. *Physics of Fluids*, Vol. 19, No. 6, p. 065103, 2007. DOI 10.1063/1.2734996
- [16] Meliga P. Reijasse P. Unsteady transonic flow behind an axisymmetric afterbody equipped with two boosters. *25th AIAA Applied Aerodynamics Conference*, 2012. DOI 10.2514/6.2007-4564.
- [17] Pain R. Weiss P. E. Deck S. Zonal detached eddy simulation of the flow around a simplified launcher afterbody. *AIAA Journal*, Vol. 52, No. 9, pp. 1967-1979, 2014. DOI 10.2514/1.J052743.
- [18] Schwane R. Numerical prediction and experimental validation of unsteady side loads on ARIANE5 and VEGA. *Journal of Spacecraft and Rockets*, Vol. 52, No. 1, pp. 54-62, 2015. DOI 10.2514/1.A32793.
- [19] Viswanath R. P. Flow Managementaw Techniques for Base and Afterbody Drag Reduction. *Progress in Aerospace Sciencies*, Vol. 32, pp. 79-129, 1996.
- [20] Tanner M. Reduction of Base Drag. Progress in Aerospace Sciencies, Vol. 16, No. 4, pp. 369-384, 1975.

- [21] Morel T. Effect of Base Cavities on the Aerodynamic Drag of an Axisymmetric Cylinder. *Aeronautical Quarterly*, Vol. 30, pp. 400-412, 1990. DOI 10.1017/s0001925900008611.
- [22] Östlund J. Damgaard T. Frey M. Side-Load Phenomena in Highly Overexpanded Rocket Nozzles. *Journal of Propulsion and Power*, Vol. 20, No. 4, pp. 695-704, 2004. DOI 10.2514/1.3059
- [23] Zucrow M. J. Hoffman J. D. Gas Dynamics. John Wiley and Sons, 1976
- [24] Sauer R. General Characteristics of the Flow through Nozzles at Near Critical Speeds. *Memorandum No.1147*, NACA, Whasington, DC, 1947.
- [25] Wilcox D. Turbulence Modeling for CFD. DCW Industries, La Canada, California, 2006.
- [26] Spalart P. R. Deck S. Shur M. L. Squires K. D. Strelets M. K. Travin A. K. A New Version of Detached-eddy Simulation, Resistant to Ambiguous Grid Densities. *Theoretical and Computational Fluid Dynamics*, Vol. 20, pp 181-195, 2006. DOI 10.1007/s00162-006-0015-0
- [27] Sagaut P. Deck S. Terracol M. *Multiscale and Multiresolution Approaches in Turbulence*. 2nd edition, Imperial College Press, 2003. DOI 10.1142/p878
- [28] Menter F.R. Two-equation eddy-viscosity turbulence models for engineering applications. *AIAA Journal*, Vol. 32, No. 8, pp 1598-1605, 1994. DOI 10.2514/3.12149
- [29] Menter F. Kuntz M. Langtry R. Ten Years of Industrial Experience with the SST Turbulence Model. Heat and Mass Transfer 4, Begell HOuse Inc., pp. 625-632, 2003
- [30] Gritskevich M. S. Garbaruk A. V. Schutze J. Menter F. R. Development of DDES and IDDES Formulations for the k-ω Shear Stress Transport Model. *Flow Turbulence Combust*, Vol. 88, pp 431-449, 2012. DOI 10.1007/s10494-011-9378-4.
- [31] Spalart P. R. Jou W. H. Strelets M. Allmaras S. R. Comments on the Feasibility of LES for Wings, and on a Hybrid RANS/LES Approach. *In Advances in DNS/LES*, pp 137-147, 1997.
- [32] Menter F. R. Kuntz M. Adaptation of Eddy-Viscosity Turbulence Models to Unsteady Separated Flow Behind Vehicles. The Aerodynamics of Heavy Vehicles: Trucks, Buses and Trains. Lectue Notes in Applied and Computational Mechanics, Springer Berlin Heidelberg, Berlin, Vol. 19, pp 339-352, 2004. DOI 10.1007/978-3-540-44419-0 30.
- [33] Ansys Inc., 275 Teechnology Drive, Canonsburg, PA 15317. Ansys Fluent Theory Guide. Release 15.0, 2013.
- [34] Ansys Inc., 275 Teechnology Drive, Canonsburg, PA 15317. Best Practice: Scale-Resolving Simulations in Ansys CFD. *Technical paper 2.00*, 2015.
- [35] Ansys Inc., 275 Teechnology Drive, Canonsburg, PA 15317. Ansys Fluent User's Guide. *Release 2021 R2*, 2021.
- [36] Liou M. S. A Sequel to AUSM: AUSM+. Journal of Computational Physics, Vol. 129, pp 364-382, 1996. DOI 10.1006/jcph.1996.0256
- [37] Sutherland W. The viscosity of gases and molecular forces. Philos. Mag., Vol. 36, pp 507-531, 1893.
- [38] Nasuti F. Onofri M. Shock Structure in Separated Nozzle Flows. Shock Waves, Vol. 19, pp 229-237, 2009. DOI 10.1007/s00193-008-0173-7
- [39] Ansys Inc., 275 Teechnology Drive, Canonsburg, PA 15317. Ansys FLUENT Meshing User Guide. Release 14.5, 2012.
- [40] Spalart P. R. Young Person's Guie to Detached-Eddy Simulation Grids. *Technical report NASA CR-2001-211032*, 2001.
- [41] Tsentis S. Goulos I. Prince S. Pachidis V. Zmijanovic V. Wind Tunnel Installation Effects on the Base Flow for a High-Speed Exhaust System. AIAA 2024-1774, AIAA SciTech Forum, Orlando, Florida, 8-13 January, 2024. DOI 10.2514/6.2024-1774.
- [42] Celik B. Ghia U. Roache P. Freitas C. Coleman H. Raad P. Procedure for Estimation and Reporting of Uncertainty Due to Discretization in CFD Applications. *Journal of FLuids Engineering*, Vol. 130, No. 7, 2008. DOI 10.1115/1.2960953
- [43] Richardson F. L. Gaunt J. The Deferred Approach to the Limit. *Philos. Trans. R. Soc. London*, Vol. 226, Ser. A, No. 636-646, pp 299–361, 1927. DOI 10.1098/rsta.1927.0008.
- [44] Dubief Y. Delcayre F. On coherent-vortex identification in turbulence. *Journal of Turbulence*, Vol. 1, No. 1, 2000. DOI 10.1088/1468-5248/1/1/011
- [45] Martelli E. Saccoccio L. Ciottoli P. P. Tinney C. E. Baars W. J. Bernardini M. Flow dynamics and wall-pressure signatures in a high-Reynolds number overexpanded nozzle with free shock separation. *Journal of Fluid Mechanics*, Vol. 895, No. 1612, 2020. DOI 10.1017/jfm.2020.280.
- [46] Spalart P. R. Detached-Eddy Simulation. *Annual Review of Fluid Mechanics*, Vol. 41, No. 1, pp. 181-202, 2009. DOI 10.1146/annurev.fluid.010908.165130.

- [47] TLumley J. L. The structure of inhomogeneous turbulent flows. *Proceedings of the International Colloquium on the Fine Scale Structure of the Atmosphere and its Influence on Radio Wave Propagation*, Moscow, 1967.
- [48] Weiss J. A Tutorial on the Proper Orthogonal Decomposition. *AIAA Aviation 2019 Forum*, AIAA 2019-3333, June 2019.
- [49] Taira K. Brunton S. L. Dawson S. T. M. Rowley C. W. Colonius T. McKeon B. J. Schmidt O. T. Gordeyev S. Theofilis V. Ukeiley L. S. Modal Analysis of Fluid Flows: An Overview. *AIAA Journal*, Vol. 55, No. 12, pp. 4013-4041, 2017. DOI 10.2514/1.J056060.
- [50] Bose C. Sarkar S. Flow Periodicity Analysis Past a Flapping Airfoil Using Proper Orthogonal Decomposition. *47th AIAA Fluid Dynamics Conference*, AIAA 2017-3647, June 2017.